Journal of Materials Chemistry A

ROYAL SOCIETY OF CHEMISTRY

PAPER

Cite this: *J. Mater. Chem. A*, 2025, **13**, 34615

# Development of single crystalline Al-doped ZnS nanodiscs as efficient photocatalysts for $H_2$ evolution reaction

Rohit R. Koli,[a] I.-Hua Tsai,[a] Yu-Bin Huang,[b] Chia-Hsin Wang,[b] Bo-Hong Liu,[b] Raghunath Putikam,[a] M. C. Lin[a] and Eric Wei-Guang Diau *[ac]

Received 12th May 2025
Accepted 20th August 2025

DOI: 10.1039/d5ta03793j

rsc.li/materials-a

The rapid photoinduced charge carrier recombination hinders the photocatalytic efficiency of binary zinc sulfide (ZS) photocatalysts. Enhanced charge separation through electronic and band structure modification *via* metal cation doping has gained much attention. Herein, aluminum (Al) doping with Pt single atoms (SAs) into single crystalline ZnS nanodiscs (Pt-AZS) with shallow defect states is reported. Rietveld refinement of XRD confirms lattice expansion with modulated electronic distribution. The additional Al-electron traps improved the lifetime of charge carriers, enhancing their interfacial transport to the metal cocatalyst, as confirmed by *in situ* XPS and time-resolved photoluminescence spectroscopy. The 1.6 wt% Pt loading on the AZS (200) facet exhibited an enhanced $H_2$ evolution rate of 17.1 mmol $g^{-1}$ $h^{-1}$ under AM1.5G irradiation with an apparent quantum yield (AQY) of 34% at 345 nm using a WB40 filter. Under UV light irradiation, Pt-AZS showed a high $H_2$ generation rate of 38 mmol $g^{-1}$ $h^{-1}$, which is two times more than that of bare Pt-ZS. This work elucidates the efficacy of Al doping with Pt SAs in a single crystalline photocatalyst to facilitate electron transport *via* suppressed band-bending at the Mott–Schottky interface, thereby boosting photocatalytic $H_2$ production.

## 1. Introduction

Rapid industrialization is causing energy crises and environmental pollution challenges. Finding an alternative eco-friendly energy source is crucial for the long-term growth of human civilization. In this regard, hydrogen ($H_2$) is a promising fossil fuel replacement owing to its renewable, carbon-neutral, energy-dense, and compressible nature for uninterrupted transportation.[1–3] However, the current rise in energy demand, poor efficiency, and ecologically harmful $H_2$ generation technologies limit the commercial use of hydrogen energy.[4,5] Alternatively, photo-induced water splitting can efficiently convert solar energy to chemical energy ($H_2$) without pollution, making it a viable and sustainable approach.[6,7]

Among inorganic photocatalysts, metal chalcogenides, including CdS, $Cu_7S_4$, $CdIn_2S_4$, and $ZnIn_2S_4$ (ZIS), have garnered interest for their excellent visible/IR-light response.[8–11] The photocatalytic properties of most of these chalcogenides are unsatisfactory due to their fast carrier recombination and structural instability from photocorrosion under full sunlight irradiation. In this regard, ZnS is a low-toxicity, UV-stable alternative with a high conduction band (CB) level beneficial for the photoreduction of water to $H_2$ ($H_2$ evolution reaction, HER) without any co-catalyst.[12,13] To enhance its performance, researchers have made significant efforts in band engineering of pristine ZnS using metal cation doping, heterojunctions, and surface modification by metal single atoms (SAs).[14–19] Among these, co-doping ZnS with Al/Ga/In and Cu resulted in a moderate enhancement of its photocatalytic activity.[20–23] In chalcogenides, anion vacancies appear to create defect states, which benefit electron trapping for accelerated photocarrier separation.[24,25] Nevertheless, excess trap states may also serve as photocarrier recombination sites, reducing photocatalytic efficacy, which can be avoided by ensuring proper defect concentration.[26] In the case of ZnS, along with S (anion) vacancies, modification of the electronic structure of photocatalysts by SA doping of metal cations can be an effective strategy for tuning the band edge position and controlled formation of donor/acceptor impurity levels.[27] Accordingly, *in situ* non-noble metal substitution at Zn sites was investigated to reduce intermediate recombination sites and to improve the photocatalytic performance of ZnS.

Previous studies have investigated $H_2$ production using ZnS doped with Cu, Ni, and Pb cations. Cu-doped ZnS has shown a shallow $Cu^{2+}$ donor level and demonstrated a high apparent quantum yield (AQY) of 3.7%, while Ni-doped ZnS showed an AQY of 1.3% at 420 nm.[28] Despite achieving a lower $H_2$ yield than that obtained using Cu-doped ZnS (yield ~6.25 mmol $g^{-1}$

[a]*Department of Applied Chemistry, National Yang Ming Chiao Tung University, Hsinchu 300093, Taiwan. E-mail: diau@nycu.edu.tw*

[b]*National Synchrotron Radiation Research Center, Hsinchu 30076, Taiwan*

[c]*Center for Emergent Functional Matter Science, National Yang Ming Chiao Tung University, Hsinchu 300093, Taiwan*

$h^{-1}$), Ni-doped ZnS (yield ~430 μmol $g^{-1}$ $h^{-1}$) remained thermally and chemically stable. The best $H_2$ generation rate of 12 mmol $g^{-1}$ $h^{-1}$ with an AQY of 12.67% was reported for Cu SA-doped ZnS with $Na_2S$ and $Na_2SO_3$ as hole scavengers.[26] However, Cu-doped ZnS suffers from photocorrosion, which can be resolved by co-doping it with metal cations like $Ga^{3+}$, $In^{3+}$ or $Al^{3+}$[29] or by surface modification with SA/NPs of noble metals like Au, Pt, and so on.[30] The reported maximum $H_2$ yield for such co-doped ZnS was below 4 mmol $g^{-1}$ $h^{-1}$.[31] Anion vacancies appear to be beneficial for introducing intermediate electron "traps" through the addition of mid-gap states. Recently, Shi *et al.* reported the highest $H_2$ yield of 17.5 mmol $g^{-1}$ $h^{-1}$ under visible light for Pt-decorated S-vacant ZIS (Pt-ZIS) with plenty of $H_2$ bubbles. However, the high cost and scarcity of the In precursor are obstacles to the practical use of ZIS in green $H_2$ production while, only S vacancies in ZnS were inefficient for significantly tuning its Fermi level and band positions. Previously, different metal-doped ZnS, including Al-doped ZnS polycrystalline structures, were studied for $H_2$ evolution with moderate improvements in $H_2$ yield.[30,32–37] The lack of favorable facet growth (particularly, having S-rich planes) can be the reason for inferior photocatalytic performance. Recently, Al-doped $SrTiO_3$ single crystalline sub-microparticles decorated with $Rh/Cr_2O_3$ nanoparticles showed quantum efficiency of almost unity for water splitting in the UV region.[38] Jia *et al.* showed the importance of directed charge transport in ferroelectric $Bi_4Ti_3O_{12}$ single crystals for overall water splitting under visible light irradiation.[39]

In the present study, enhanced photocatalytic HER performance using co-cationic doping in ZnS nanodiscs (NDs) is reported. A less reactive $Al^{3+}$ cation was chosen as a dopant to avoid secondary phase formation and to ensure single crystalline growth along the (111) plane of the ZnS NDs in which the $Al^{3+}$ cations occupy $Zn^{2+}$ sites and the S-rich (200) plane directed the ZnS growth. A high $H_2$ evolution rate of 17.1 mmol $g^{-1}$ $h^{-1}$ with an AQY of 34% at 345 nm was achieved by Pt SAs anchored to Al-doped ZnS (Pt-AZS) NDs. The HER rate is comparable to that of the Pt-ZIS system, and it is also 30% higher than the previous record for the Cu-doped ZnS system.[26] In the photochemical reaction chamber with both UV-A and UV-B irradiations, the Pt-AZS photocatalyst attained a remarkable HER yield of 38 mmol $g^{-1}$ $h^{-1}$, which is almost two times greater than that of the Pt-ZnS photocatalyst without Al-doping.

# 2. Experimental

### 2.1. Preparation of ZnS microdiscs by a hydrothermal method

ZnS chalcogenide microdiscs (MDs) were synthesized by a moderately high-temperature hydrothermal method. The synthesis of ZnS MDs was carried out by dissolving 2.5 mmol of zinc acetate (Zn $(CH_3CO_2)_2 \cdot 2H_2O$) and 80 mmol of thioacetamide ($C_2H_5NS$) in 25 mL of deionized (DI) water separately to obtain colorless solutions. These zinc acetate (ZnAc) and thioacetamide (TAA) solutions were thoroughly mixed for 15 min under magnetic stirring and transferred to a 120 mL Teflon-lined autoclave. The final mixture volume was increased to 100 mL by the addition of DI water. Then this Teflon lined autoclave was kept in a muffle furnace pre-programmed for 180 °C with an initial temperature rise of 12 °C $min^{-1}$, followed by heating at 180 °C for 12 h. After natural cooling, the product was washed with DI water and ethanol three times and dried in a vacuum oven at 60 °C overnight. The dried sample was ground in a mortar and pestle and denoted as ZS0 for further study.

### 2.2. Preparation of ZnS and AlSA-ZnS nanodiscs by the hydrothermal method

The synthesis of ZnS nanodiscs (NDs) was carried out by using a mixture of 2.5 mmol of ZnAc, 80 mmol of TAA, and 10 mmol of trisodium citrate dihydrate ($C_6H_5Na_3O_7 \cdot 2H_2O$), *i.e.*, NaCt, in DI water. This mixture was then hydrothermally treated at 180 °C in a Teflon-lined SS autoclave for 12 h. After cleaning and vacuum drying, the sample was abbreviated as ZS. In a similar way, Al-ZnS was hydrothermally synthesized by dissolving 2.5 mmol of ZnAc, 80 mmol of TAA, 10 mmol of NaCt and 5 mmol of anhydrous $AlCl_3$ in 25 mL of DI water separately. These solutions were then added to a 120 mL Teflon-liner under magnetic stirring. The remaining cleaning process was similar to that of ZS. The vacuum-dried Al-doped fine powder sample was denoted as AZS.

# 3. Results and discussion

### 3.1. Crystal growth and structure analysis

The hydrothermal synthetic procedures of ZS and AZS photocatalysts with ND shape and thickness below 50 nm are schematically shown in Fig. 1. The introduction of a reducing agent along with $Al^{3+}$ cations (Zn : Al = 1 : 1) significantly lowers the nanoparticle size to 105 nm (Fig. S3c).

In AZS, the presence of two metal cations created S vacancies and as the formation energy of the compound for Al-substituted Zn sites is found to be minimal, Al preferably occupies some of these Zn positions.[40] To confirm the lowest formation energy of Al substitution and the modification in electronic structure by lattice distortion, we performed possible ways of introducing an Al atom into the ZnS (zinc blende) $\bar{F}43m$ structure, where the formation energies were computed using DFT calculations implemented in the Vienna *ab initio* simulation package (VASP).[41] The 1.6 wt% Pt SAs were photodeposited on AZS by injecting aqueous $H_2PtCl_6$ (50 mg $mL^{-1}$) into an aqueous dispersion of 2.5 mg AZS under AM 1.5G simulated light illumination.

Spherical aberration-corrected scanning transmission electron microscopy (Cs-corrected STEM) measurements were conducted on AZS and Pt-AZS to determine sample morphology and the configuration of the Pt co-catalyst (Fig. 2).

The optimized NaCt-assisted AZS sample had a uniform ND morphology with a diameter of 105 nm (Fig. 2a). The EDS line scan profiles measured at the middle position (in bulk) and at the edge of a single AZS nanoparticle differ in their elemental distribution (Fig. 2b and c). The uniform distribution of Zn and S in the EDS line scan measured at the middle (position 1) along with the gradual reduction in net counts measured at the corner

 

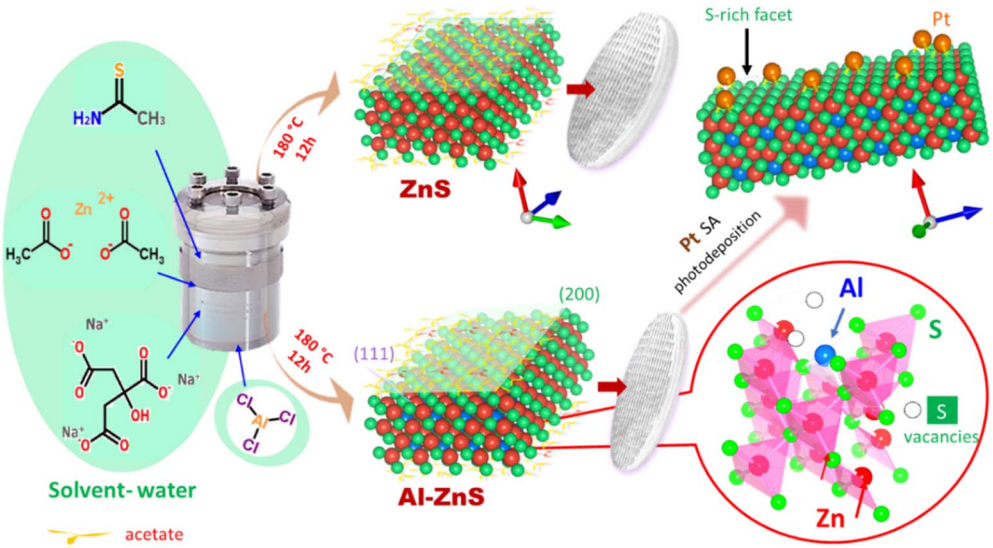


Fig. 1 Schematic presentation of the hydrothermal synthesis of ZnS (ZS) and Al-ZnS (AZS) nanodiscs with the proposed crystal structures.

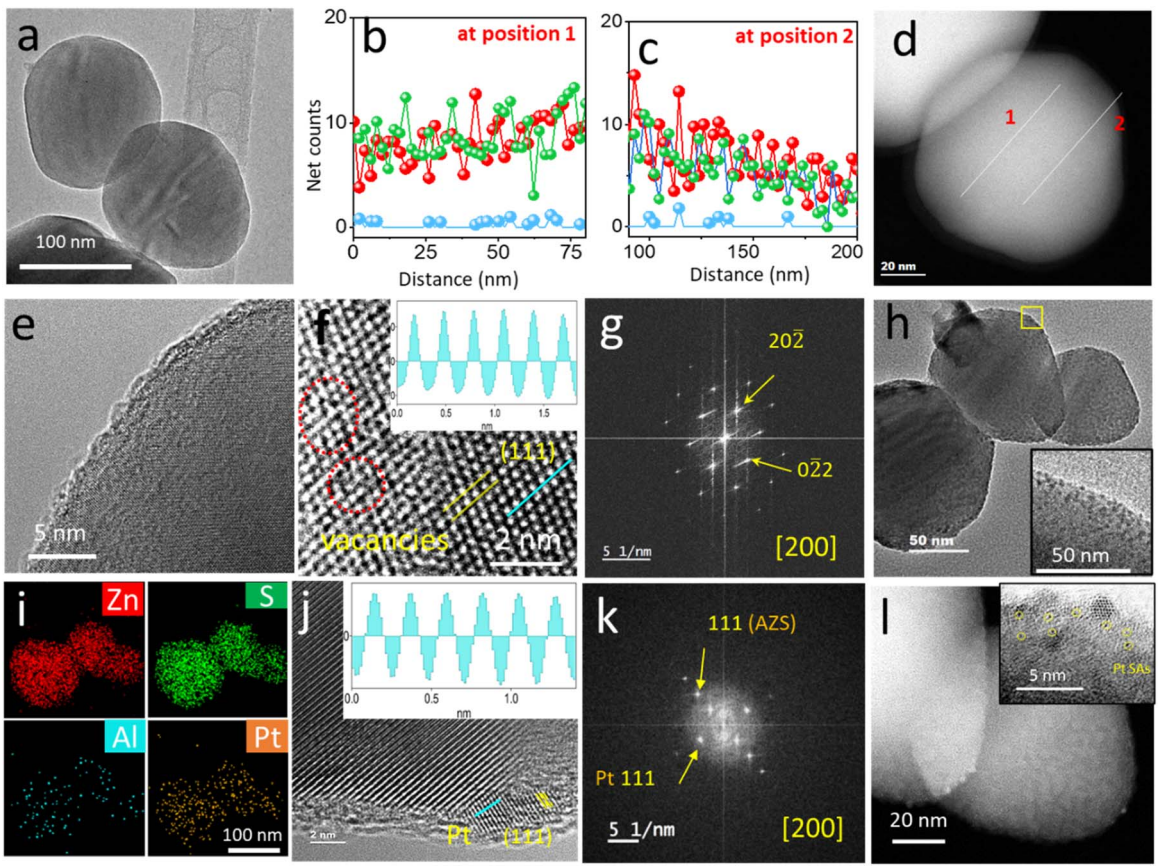


Fig. 2 (a) TEM image of AZS; (b and c) EDS line scan profiles of AZS measured at the middle (position 1) and corner position (position 2) of AZS, respectively. The plots for Zn, S and Al are shown in red, green and blue colors, respectively. (d) The dark field-TEM image of AZS; (e) HRTEM image of AZS; (f) STEM image of AZS showing the atomic arrangement. The inset shows the line profile for interplanar spacing of (111) planes of AZS. (g) Simulated SAED pattern of the STEM image of AZS in (f); (h) TEM image of Pt-AZS. The inset image shows Pt SA decoration on AZS. (i) Elemental mapping of Zn, S, Al and Pt in Pt-AZS; (j) STEM image of Pt-AZS showing the Pt SA sites on AZS. The inset shows the line profile for interplanar spacing of (111) planes of Pt. (k) Simulated SAED pattern of the STEM image of Pt-AZS in (j); (l) the dark field-TEM image of Pt-AZS. The HRTEM image in the inset shows Pt SA sites (encircled black dots) on AZS.

(position 2), confirms the ND morphology of AZS. Such a nanodisc surface can benefit from the preferential growth of Pt SA sites. The corresponding positions are shown in a high-angle annular dark field (HAADF) STEM image of AZS (Fig. 2d). The high-resolution TEM (HRTEM) image in Fig. 2e and the atomic arrangement in STEM (Fig. 2f) of AZS show zinc blend ZnS structures (JCPDS card no. 65-0309)[42] grown in a single crystalline orientation along the (111) lattice plane with an interplanar spacing ($d$) of 0.31 nm (the line profile for interplanar distances from HRTEM are shown in the inset of Fig. 2f).[43] This single crystalline growth is also confirmed from the simulated selected area electron diffraction (SAED) pattern of the STEM image of AZS (Fig. 2g). As seen from the TEM image of Pt-AZS (Fig. 2h), AZS retains its morphology even after the Pt photodeposition process. The STEM image in Fig. 2h reveals the growth of tiny single crystalline Pt nanocrystals (~2 nm) on the (200) lattice plane of AZS with uniform surface decoration, as seen in the inset of the TEM image in Fig. 2h.

In Fig. 2i, the EDS mapping of Pt-AZS (the corresponding TEM image is shown in Fig. 2h) shows a uniform elemental distribution of Zn, S, Al, and Pt, which supports the formation of disc-like shape of AZS. No degradation or oxidation is observed for Pt-AZS after photodeposition which is confirmed from the O level in its EDS spectrum (Fig. S3f). The growth of Pt on the S-rich (200) plane of AZS at the atomic scale is shown in the STEM image of Pt-AZS (Fig. 2j). The inset of Fig. 2j represents the line profile for a $d$-spacing of 0.25 nm corresponding to the (111) lattice plane of Pt, which is also reflected in its SAED pattern (Fig. 2k).[44] Fig. 2l shows the HAADF-STEM image of Pt-AZS. Because the contrast is proportional to the square of the atomic number, the uniformly distributed tiny bright spots that emerged in the dark-field TEM of Pt-AZS indicate the deposition of Pt SA sites.[45]

The generalized gradient approximation (GGA) in the formalism of Perdew–Burke–Ernzerhof (PBE) was adopted to describe the electronic exchange-correlation energy. The projector augmented wave (PAW) pseudo-potentials were chosen to describe ionic cores.[46,47] We utilized the standard PBE functional method which correctly improved the van der Waals interactions using the Becke–Jonson damping potential with the DFT-D3 method.[48] The convergence criterion for the self-consistent iteration was set to 10–5 eV. The calculations were carried out with a plane-wave basis set cutoff energy of 520 eV and a Gaussian smearing method with a width of 0.05 eV was applied in order to ensure well-converged total energy and force values.

The structural optimization of the cubic $\bar{F}43m$ space group (216) of the ZnS crystal structure was performed with a $k$-point mesh with the Monkhorst–Pack scheme set to 4 × 4 × 4. The predicted lattice parameters of unit cell was 5.383 Å, in good agreement with the experimental data ($a = b = c = 5.409$ Å). To model the Al-doped material, we considered a ZnS supercell (2 × 2) model containing 32 ZnS units with cell parameters $a = b = c = 10.760$ Å. We considered two possible ways of introducing Al-doping into the lattices of ZnS. The first was a Zn or S atom substituted with an Al atom (denoted as $Al_{Zn}$ and $Al_S$); the second was an Al atom situated at an interstitial position (denoted as $Al_{int}$). To characterize the stability of the dopant in substitutional and interstitial configurations in ZnS, we calculated the formation energies ($E_{form}$) using the following relation $E_{form} = E(\text{Al-ZnS}) - E(\text{ZnS}) - \mu(\text{Al}) + \mu(\text{Zn})$, where $E$(ZnS) and $E$(Al-ZnS) are the total energies of the pristine ZnS supercell and doped ZnS. The quantities $\mu$(Al), $\mu$(Zn), and $\mu$(S) represent the chemical potentials of aluminum and the substituted Zn or S atom in the host lattice, respectively. The chemical potentials for doping $\mu$(Al), $\mu$(Zn), and $\mu$(S) were calculated from Al, α-solid S8, and Zn bulk metal, respectively. The formation energies of dopant atoms in different configurations were calculated by using the DFT-D3 method and are presented in Fig. 3b. The supercell model and partial geometries of structurally optimized Al-doped ZnS are shown in Fig. 3a. We observed that substitution of Zn with an Al atom in Al-ZnS expands the lattice.

We theoretically investigated the formation energy of Al substituted at the Zn sites in ZnS, which is 0.93 eV, relatively more stable than other doping sites. The substituted optimized supercell lattice constant of the axis slightly increased to 10.793 Å from 10.760 Å in ZnS (see Fig. 3a). In our calculations, we observed that the formation energy of Al substituted at the S site in the ZnS model (5.85 eV) is higher than that of Al substituted at the Zn site (0.93 eV). For comparison, we also calculated the Zn defect formation energy in ZnS, which is 3.58 eV, much lower than that of the S defect (4.15 eV). In the Al atom interstitial model ($Al_{int}$), we investigated the effect of Al doping located interstitially at various places in between S and Zn atoms in the ZnS supercell, and their formation energy was found to be 4.56 eV. These results indicate that Al substitution at Zn sites in ZnS is relatively more stable than other doping sites and therefore it represents a more favorable doping site. Moreover, the electronic structure of $Al_{Zn}$-ZnS (*i.e.*, AZS) is modified due to the lattice expansion with the Zn–S bond length increasing from 2.33 Å to 2.34 Å. A similar increase in Zn–S bond distance was observed from the Rietveld refinement of experimental XRD data (discussed later).

A 2.2% Al doping level was found to be sufficient to induce lattice distortion of the ZnS unit cell (XRD pattern in Fig. 3c and d). These XRD patterns show sharp diffraction peaks indexed to the $F$-43$m$ group of the zinc blend ZnS structure, which enables sufficient space for doping by bigger-sized cations. In AZS (Fig. 3d), the intense peak at 28.4° of the (111) lattice plane and the small peak at 32.9° of the (200) lattice plane indicate preferential crystal growth along the (111) plane bounded by the (200) facet plane and contribute to the nanodisc morphologies derived from the HRTEM analysis. Since the atomic radius of Al (143 pm) is slightly bigger than that of Zn (137 pm), it induces lattice expansion in the cubic ZnS unit cell. Therefore, an unambiguous peak shift toward lower angles was observed (Fig. 3e). The resultant increase in lattice constants (Fig. 3f and g) is extracted from the XRD Rietveld refinement of both ZS and AZS (Fig. 3c and d). pristine ZnS showed the $F$-43$m$ space group, where Zn occupies the 4α:0 0 0 and S occupies the 4b:$\frac{1}{4}$ $\frac{1}{4}$ $\frac{1}{4}$ Wyckoff positions.[49] The zinc blend wurtzite crystal structure allows sufficient space for cation doping, in which three possible sites are available for Al-doping, namely the Zn-site, the S-site and the interstitial position.[40] However, Al doping in the

 

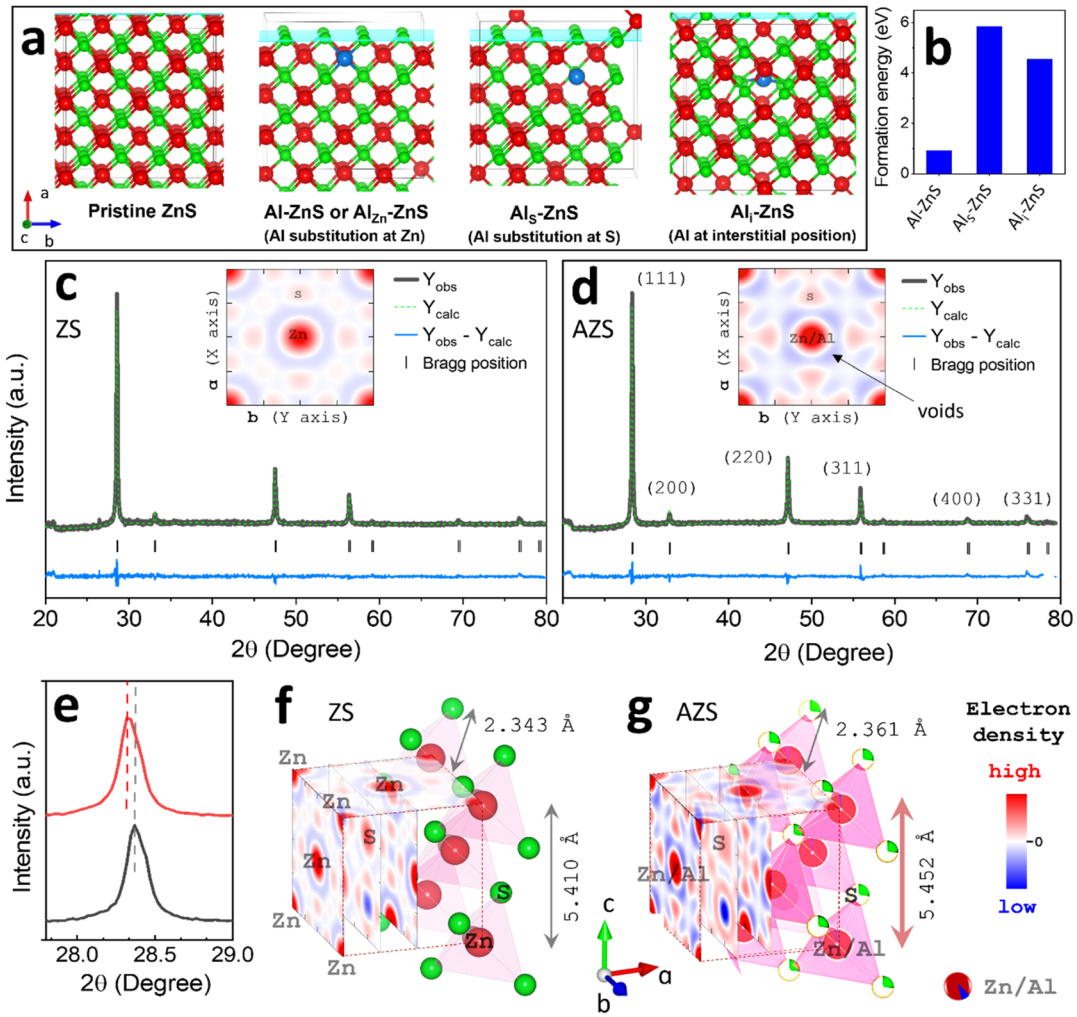


Fig. 3 (a) Supercell of pristine ZnS and Al-doped ZnS with Al at the substitutional position of Zn, substitutional position of S and interstitial position, respectively, (b) histogram plot for comparison of their formation energies using DFT calculations, (c) Rietveld refinement of XRD data of ZS; (d) Rietveld refined data of AZS with Al substitution at Zn 4$\alpha$ sites. The insets of (a) and (b) show EDMs at $x = 0$ along the [100] axis for ZS and AZS, respectively. (e) Enlarged XRD (111) peaks showing a lower angle shift for AZS than for ZS; (f and g) the distributions of electron densities in unit cells of ZS and AZS, respectively.

interstitial position is less favorable and leads to an unstable phase. During the formation of the zinc blend structure, the 4$\alpha$ sites (corresponding to Zn) are available for $Al^{3+}$ cation occupation, and therefore refinement was performed by considering Al SA doping at some of the 4$\alpha$:0 0 0 positions. The fitting converged well after the inclusion of the crystalline anisotropy coefficient for the dominant (111) plane. A 2.2% doping of relatively bigger Al cations causes a slight shift of (111) peaks towards smaller angles, indicating expansion in the unit cell with an increment of 0.042 Å in each lattice constant, as seen from Fig. 3d and e. An increase in Zn–S bond length from 2.343 Å to 2.361 Å upon Al SA doping is observed, which makes the Zn–S bond in AZS weaker than that in ZS. Evidence of SA doping was also obtained from EPR spectra of ZS and AZS, where AZS showed weaker EPR intensity compared to ZS due to the Zn vacancy filling by Al atoms. The Al SA doping lowers the interaction between vacancies (Fig. S4a).[26]

Fourier electron density mapping (EDM) of ZS and AZS was generated by taking projections along the [100] axis at different cross-sections of the unit cell with contour color representing the strength of electron densities. From the inset of Fig. 3c, higher electron density is observed around cations (Zn/Al) than that around S (warm region in red color), while the lowest electron density is seen in neighboring crystal voids (cool region in blue color).[50,51] In AZS, the increase in Zn–S bond length enhanced the electron charge distribution around atoms and also increased the void volume (inset of Fig. 3d). Eventually, this affects the band edge positions and optical properties of AZS, which will be elaborated on in the next section. In hydrothermal synthesis, $Al^{3+}$ was found to be a good option for doping due to its lower tendency to form secondary phases with S at modest reaction temperatures. Furthermore, $Al^{3+}$ can introduce additional defect levels near the CB that may delay carrier recombination. Note that no lattice distortion was found after the

addition of NaCt (a reducing agent) during ZnS synthesis, which is confirmed by comparing the XRD patterns of ZS0 (Fig. S4b and c) and ZS (Fig. 3c) and revealing the same lattice parameters with identical EDM.

X-ray photoelectron spectroscopy (XPS) was utilized to determine the chemical states and surface element composition of ZS and AZS (Fig. S5–S7). Usually, the incorporation of dopants can increase the charge carrier density in photocatalysts, which ultimately affects their XPS peak positions.[26] After ~12% Cu doping in ZnS, Liu *et al.* observed 0.29 eV and 0.19 eV shifts towards higher binding energy (BE) in Zn 2p and S 2p XPS peaks, respectively, indicating the introduction of additional charge carriers. While, under light irradiation, decreases in BEs of these peaks were observed due to the transfer of photoexcited electrons to surface metal atoms/cocatalysts *via* the Mott–Schottky interface.[52] Previous investigations have shown that SA sites may extract photogenerated electrons and lower the electron density (charge carrier) in the photocatalyst, while the intrinsic doped metal atoms serve as electron-transfer bridges with increased charge density.[26,53,54] The present Pt-AZS photocatalyst includes both intrinsic metal atom doping and Pt SA decoration on the AZS surface. Specifically, after comparing the core levels of ZS and AZS, the BE intervals between the $2p_{3/2}$ and $2p_{1/2}$ peaks for both Zn and S remained unchanged, which confirms the intactness of the parent zinc blend structure. The quantitative XPS analysis of ZS and AZS survey spectra revealed that Al atoms preferentially replace adjacent S atoms to create S vacancies (Fig. S5). As shown in the XPS scan spectrum of Pt-AZS (Fig. S7c), the peaks observed at 71.4 eV and 76.8 eV are associated with the $4f_{7/2}$ and $4f_{5/2}$ orbitals of Pt, respectively, while a minor peak at 73.9 eV corresponding to the Al 2p core level confirms a small amount of Al doping in Pt-AZS. The chemical states are determined from the observed BEs of the core level of elements. The BE peak at 1021.3 eV corresponds to the Zn $2p_{3/2}$ core level with a +2 oxidation state, while the major peak at 161.3 eV confirms S $2p_{3/2}$ with a −2 oxidation state. A small peak observed near 73.9 eV reveals the Al 2p core level with *a* +3 oxidation state. Similarly, the characteristic peak at 71.4 eV, corresponding to Pt $4f_{7/2}$, confirms the deposition of metallic Pt ($Pt^0$) on AZS, while the BE peak at 76.8 eV, corresponding to Pt $4f_{5/2}$, indicates *a* +2 valency.

### 3.2. Photoactivation of Pt-AZS in water vapor: an *in situ* XPS study

The *in situ* XPS measurements were conducted under light irradiation to investigate the relative kinetics of photogenerated electrons in the Pt-AZS system (Fig. 4). The XPS measurements performed in dark (W) and under light irradiation (WL) with corresponding plots for Zn, S, O, and C peaks are shown in Fig. 4a–d, respectively. *In situ* measurements performed every 2 hours are plotted as WL-4h, WL-6h and WL-8h, as shown in

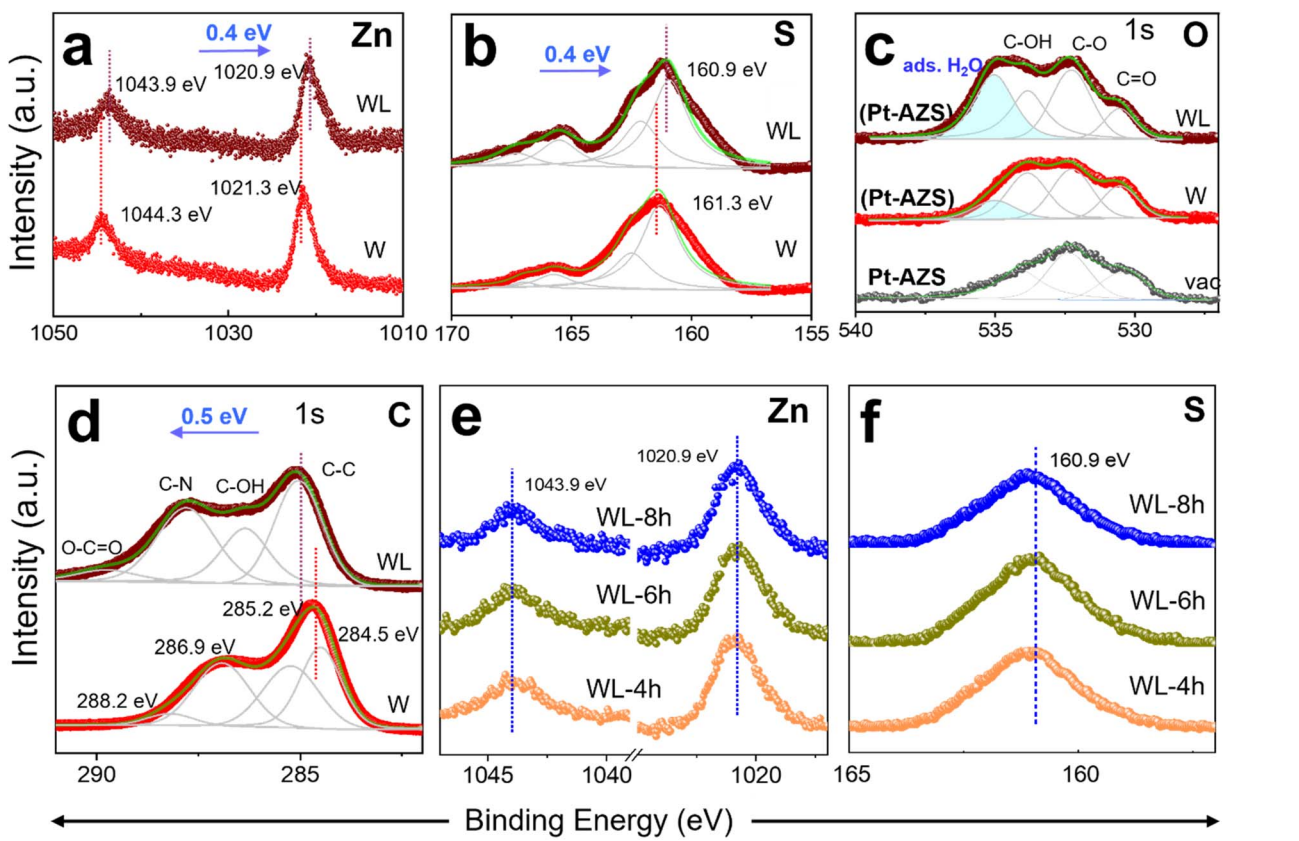


Fig. 4 The *in situ* XPS spectra for (a) Zn 2p, (b) S 2p, (c) O 1s and (d) C 1s in the presence of water vapor (W) and under light irradiation (WL) on a TEOA adsorbed Pt-AZS film. (e and f) The XPS peak positions of Zn and S under light after 4, 6 and 8 h of irradiation.

Fig. 4e and f. In Pt-AZS, as only 1.6 wt% Pt was utilized for decoration, the low-concentrated Pt SA sites did not influence the metal-sulfide XPS peaks appeared near 161.3 eV. When comparing XPS spectra of bare Pt-AZS with those under light irradiation, both Zn $2p_{3/2}$ and Zn $2p_{1/2}$ peaks were equally shifted by 0.4 eV towards lower binding energies compared to those under dark conditions (Fig. 4a). A similar 0.4 eV shift to lower energy was detected in S 2p core levels. These downshifts in binding energies predict that the photogenerated electrons are more likely to be trapped by defect levels (S vacancies and shallow defect levels acting as electron gathering centers) and then transferred to the Pt SA sites on the S-rich (200) facet of Pt-AZS.[55] The two minor peaks observed at 165.7 eV and 167 eV in Pt-AZS (Fig. 4b) are attributed to –C–($SO_2$)–C sulfone bridges.[56] Notably, throughout the *in situ* photocatalytic study, water vapor was generated by controlled water sprinkling in the XPS chamber at a fixed vacuum level ($\sim 2 \times 10^{-2}$ Torr). In the dark, the O 1s core level exhibited two peaks at 530.5 eV and 532.2 eV, corresponding to the C=O and C–O species of TEOA, respectively.[57] The XPS peak at 533.8 eV is associated with C–OH. Upon continual purging of water vapors, an additional peak appears at 535.0 eV, which steadily increases in intensity over time.[58,59] The effect of light irradiation on adsorbed TEOA was investigated by monitoring *in situ* XPS spectra of O 1s (Fig. 4c), C 1s (Fig. 4d), and N 1s core levels (Fig. S7d). The positions of the intense peaks of O 1s and N 1s remained unshifted after light exposure, revealing chemical stability of the TEOA molecules. In contrast, a lower BE shift of 0.5 eV in C 1s occurred due to the capture of photoinduced holes from the VB of Pt-AZS to produce $TEOA^+$. This *in situ* XPS analysis explains the improved photogenerated electron transfer mechanism from the CB of AZS to Pt SA sites. In addition, the shallow trap levels created by Al-doping can also contribute to photogenerated electron harvesting and subsequent transfer to Pt sites, which will be discussed in the following section. These shifts in BEs remained unchanged on continuous light exposure (Fig. 4e and f), indicating chemical stability of Pt-AZS in full light spectra.

### 3.3. Photocatalytic $H_2$ evolution performance

The photocatalytic $H_2$ evolution performances of Pt-decorated pristine ZnS (ZS0 and ZS) and Al-ZnS (AZS) in an aqueous solution of 10 vol% TEOA (sacrificial agent) were investigated under AM 1.5G solar spectral irradiation (Fig. 5). Fig. 5a and b exhibit an enhancement in $H_2$ production after Al-doping. The Pt-loaded pristine photocatalysts ZS0 and ZS showed low $H_2$ production yields of 2.6 and 11.3 mmol $g^{-1}$ $h^{-1}$, respectively, whereas S-vacant Pt-AZS achieved an improved $H_2$ evolution rate of up to 17.1 mmol $g^{-1}$ $h^{-1}$. Pt-AZS exhibits increased photocatalytic activity due to the rapid photocarrier separation caused by the S vacancies acting as electron traps. Additionally, Pt SA sites boosted $H_2$ evolution activity by increasing electron extraction from AZS to Pt SAs through the Mott–Schottky heterojunction under light irradiation. Herein, 1.6 wt% Pt deposition was observed on the AZS surface (confirmed from EDS analysis). After simulated solar irradiation, the prepared Pt-AZS was recycled several times and studied for its $H_2$ evolution performance (Fig. S9). For the comparison purpose, under similar conditions, the $H_2$ evolution performance of $TiO_2$ nanoparticles (~20 nm, P25) was investigated, which showed

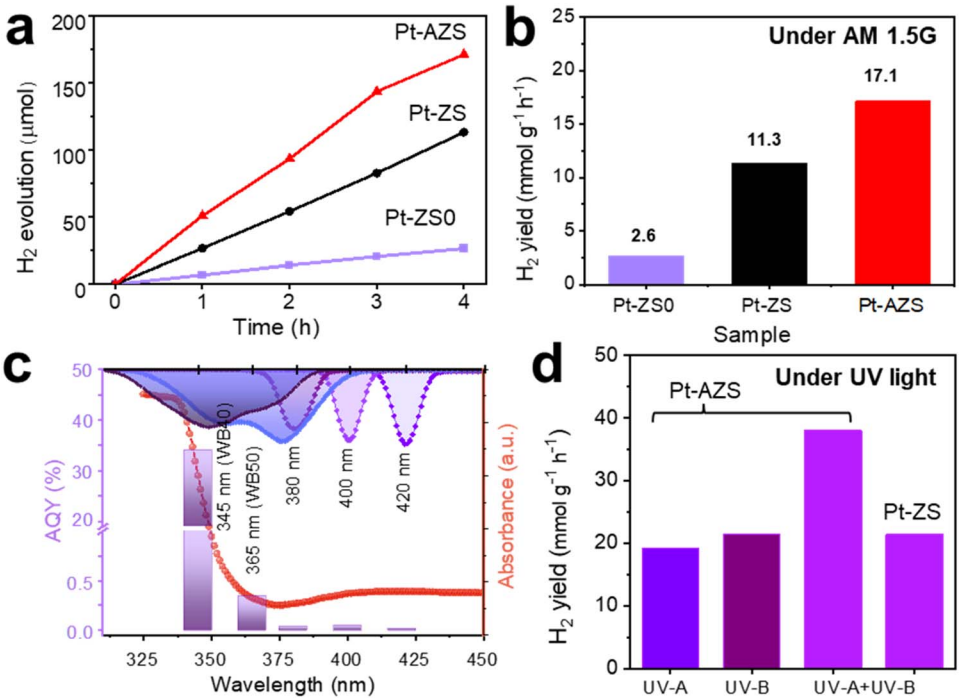


Fig. 5 (a) $H_2$ evolution performance with time; (b) rate of $H_2$ production by Pt-ZS0, Pt-ZS and Pt-AZS under AM1.5G light irradiation; (c) apparent quantum yield (AQY) at different wavelengths using narrow band (NB) and wide band (WB) spectral filters; (d) the $H_2$ evolution rates of P-ZS ad Pt-AZS under UV-A, B irradiation.

only a 13.5 mmol $g^{-1}$ $h^{-1}$ yield. The photocatalytic quantum efficiencies of Pt-AZS were investigated by measuring photocatalytic $H_2$ evolution using monochromatic band-pass (BP) filters at different wavelengths ($\lambda$ = 420, 400, 380, 365 (WB50), and 345 (WB40) nm). The total $H_2$ evolution and the total number of photons transmitted by these band-pass filters are provided in Table S2. Accordingly, the AQY of Pt-AZS for these wavelengths was calculated (the details of the calculations are provided in the SI), and the $H_2$ evolution rate histograms are shown in Fig. 5c.

The transmitted light intensity profiles of the BP filters are also plotted on the inverted *X*-axis. The observed AQYs are 0.02% (420 nm), 0.05% (400 nm), 0.04% (380 nm), 0.35% (365 nm), and 34% (345 nm), with these histograms coinciding with the UV-Vis absorbance spectra. These values demonstrate the excellent UV activity of Pt-AZS, and therefore, an $H_2$ evolution study was conducted in a two-channel photoreactor with UV-A and UV-B lamps (Fig. S10). As depicted in Fig. 5d, Pt-AZS showed the highest $H_2$ evolution rate of 38 mmol $g^{-1}$ $h^{-1}$; in contrast, under the same experimental conditions, Pt-ZS has reached only 21.4 mmol $g^{-1}$ $h^{-1}$, indicating the superior HER activity of Pt-AZS in the UV region. The stability of Pt-AZS was confirmed by conducting $H_2$ evolution experiments for 48 h under simulated solar illumination. After 48 h the sample color remained the same whereas the TEOA solution color changed to yellow due to the formation of $TEOA^+$ (Fig. S11). This post-photocatalytic sample, denoted as Pt-AZS-48 h, was further characterized by XRD, XPS, TEM and EDS (with mapping). The XRD pattern of Pt-AZS-48 h showed no change in peak positions which indicates no degradation of the sample after Pt-deposition (Fig. S12). The stability of the sample was visualized from the EDS spectrum where no O-peak appeared after prolonged use in solvent under light illumination (Fig. S13). Uniform elemental distribution was observed from EDS mapping (Fig S13c). The O-content in the pre- and post-photocatalytic reaction was determined by measuring XPS spectra of AZS, Pt-AZS and Pt-AZS-48 h on C-tape (Fig. S14). The ratio of C/O describes the O content and hence the stability of the prepared samples. Interestingly, under all these conditions, C/O remained nearly the same except for highly Al doped AZS* where, C/O was 0.159 indicating a possible secondary oxide phase (Table S3). Furthermore, the EDS spectra of above samples with elemental mapping confirms minimal O content with uniform distribution of other elements (Fig S15).

### 3.4. Band structure, charge-transfer dynamics and photocatalytic mechanism for $H_2$ evolution

To understand the source of enhanced photocatalytic activity of AZS for $H_2$ evolution, fundamental processes such as absorption/PL spectra, charge separation, and photogenerated electron transfer were further studied. Ultraviolet photoelectron spectroscopy (UPS) was utilized to predict the band structures of ZS and AZS. By using the formula $\Phi = h\nu - (E_{cutoff} - \Phi_{Au})$, work functions ($\Phi$) for ZS and AZS were determined to be −2.89 eV and −3.37 eV, respectively, where $h\nu$ is the photon energy 21.22 eV, $E_{cutoff}$ is cutoff energy, and $\Phi_{Au}$ is the work function of Au as determined by UPS (Fig. S16b).[30,60] Using values of $\Phi$ and binding energies ($E_b$) from Fig. S16c, the valence band maxima (VBM) are estimated to be −6.36 eV for ZS and −5.77 eV for AZS.[61] Accordingly, their conduction bands are determined by adding $E_g$ to the VBM values. The 2.2% Al-doping upshifted the VB (and CB) towards the vacuum level by 0.59 eV compare to pristine ZS, while the Fermi level decreased by 0.48 eV (Fig. S16d). For UPS of pristine ZnS (ZS*), the cutoff energy positions are shown in Fig. S17.

The defect states can also contribute in the quenching of carrier recombination. Photoluminescence (PL) spectroscopy can be applied to investigate these defect states from the analysis of radiative recombination of photogenerated electrons and holes.[62] As illustrated in the PL spectra of AZS (Fig. S18a and S6a), higher excitation wavelengths ($\lambda_{ex}$ > 340 nm with energy lower than $E_g$) enhance the blue emission (425–470 nm), while suppressing broad orange emission near 600 nm. Particularly, at low excitation energies (below $E_g$), the increase in intensities of shorter wavelength PL peaks observed over the range of 420–520 nm indicates a considerably higher recombination rate of photogenerated electrons, providing evidence of poor charge separation. The PL peak intensities of AZS are weaker than those of pristine ZS, attributed to the suppression of charge recombination after Al-doping. The incorporation of Al in ZnS can efficiently separate the photoexcited charge carriers and improve the photocatalytic efficiency of the photocatalyst by quenching the recombination of photogenerated electrons by means of intermediate defect levels. Upon comparing the deconvoluted PL spectra of ZS and AZS obtained at 340 nm excitation, an additional peak emerged at 535 nm, while the dominant peak at 606 nm was suppressed after Al doping (Fig. 6). As shown in Fig. 6b, the PL spectra indicate significant changes due to Al doping. The emissions are explained by a simplified picture of different defect centers, namely, S vacancies ($V_S$), Al SA substitutional defects ($I_{Al}$), and zinc defects ($V_{Zn}$). The three blue emissions observed at 425, 441, and 465 nm are attributed to radiative de-excitation of photogenerated electrons from the defect states of S vacancies, while a green emission at 501 nm can originate from the direct transition from the CB edge to the $V_{Zn}$ level.[27] Similarly, the dominant broad orange emission peak at 606 nm is assigned to the transition of electrons from interstitial Zn ($I_{Zn}$) defect states to $V_{Zn}$ (deep level transitions). Usually, cation substitutional defects ($I_{Al}$) are located near the CB, and the new peak that appeared at 535 nm can arise from the self-activated luminescence *via* $I_{Al}$–$V_{Zn}$ transitions (shallow trap-acceptor level transitions), which is a characteristic peak of substitutional doping.[37,63] Furthermore, the suppression of the 606 nm peak emphasizes a substantial reduction in $I_{Zn}$ states and subsequently enhances electron trapping at $V_S$ states.

To elucidate the charge carrier dynamics, the TRPL decay profiles of ZS and AZS were obtained by laser excitation at $\lambda_{ex}$ = 375 nm. The TRPL spectra of thin films shown in Fig. 6c are well fitted to the tri-exponential decay function $I(t) = A_1e^{-t/\tau_1} + A_2e^{-t/\tau_2} + A_3e^{-t/\tau_3}$, where $I$ represents the PL intensity, $A_i$ is the percent contribution, and $\tau_i$ ($i$ = 1–3) represents lifetime components. The estimated parameters derived from the fitted

 

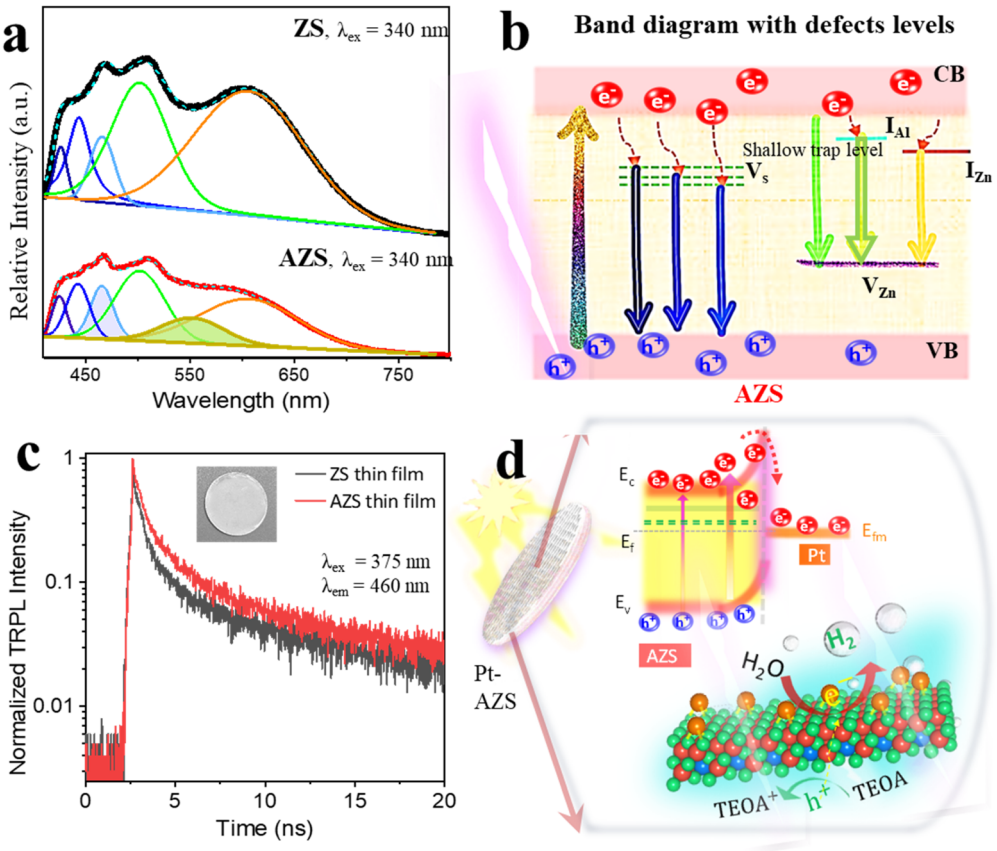


Fig. 6 (a) Comparison of PL emission spectra of ZS and AZS at $\lambda_{ex} = 340$ nm; (b) schematic of the energy level diagram showing shallow trap levels, S vacancies and zinc defect states; (c) TRPL decay curves of the thin film samples; (d) photocatalytic charge transfer mechanism in the AZS/Pt Mott–Schottky junction under light irradiation in 10 vol% TEOA aqueous solution.

curves are demonstrated in Table S4. The average lifetime (amplitude weighted) of AZS is 2.50 ns, which is longer than that of ZS (2.26 ns). Moreover, the contribution of long-lived excited electrons (with the longer lifetime component $\tau_3$) in AZS is higher (45%) than in ZS (20%), indicating preferential migration of photogenerated carriers to the electron traps for efficient charge transport rather than recombination, which is attributed to increased defect levels after Al-doping. Based on the fractional amplitudes of lifetime components, a shorter PL lifetime of non-radiative transition represents fast transfer of photogenerated electrons to defect states prior to radiative decay. Furthermore, the electron transfer dynamics can be analyzed without interrupting long-lived radiative recombination by conducting TRPL measurements of catalysts in aqueous suspension (Fig. S18b). The observed TRPL data follow a bi-exponential trend $I(t) = A_1e^{-t/\tau_1} + A_2e^{-t/\tau_2}$ with average PL lifetimes of 1.63 ns and 1.95 ns for ZS and AZS, respectively. Table S5 provides the estimates of amplitudes and lifetime components for aqueous dispersions of ZS and AZS. In aqueous suspension of photocatalysts, the photoexcited electrons with longer lifetimes ($\tau_3$) are efficiently transported to Pt SA sites *via* the Schottky interface for water reduction. Therefore, only electrons with shorter lifetimes ($\tau_1$ and $\tau_2$) undergo recombination. The short lifetime component $\tau_1$ could arise from non-radiative transitions from the CB to different trap levels near the CB, while component $\tau_2$ corresponds to recombination of photogenerated electrons from $V_S$ to the VB.

Based on the above discussion, the mechanism of photoexcitation and electron transport from the CB of AZS to Pt SAs through the Mott–Schottky junction is shown in Fig. 6d; two possible $H_2$ production mechanisms are shown in Fig. S19. Upon light irradiation on aqueous dispersion of AZS, electrons are excited to the CB, while holes are scavenged by TEOA, forming $TEOA^+$ ions. In AZS, the shallow defect levels and Vs states efficiently trap the photogenerated electrons and delay their recombination while downshifting in $E_f$ reduces band bending at the Mott–Schottky junction, enhancing the probability of electron transport to the Pt SA sites. On the other hand, the elevated conduction band (CB) of AZS provides a greater reduction capability for the photogenerated electrons and enhances the formation of molecular hydrogen compared to undoped ZS. These favorable modifications in the AZS band structure lead to enhanced $H_2$ evolution under both AM1.5G and UV light irradiation without degradation of its single crystallinity. The additional shallow donor states introduced by Al-doping enhance electron trapping and increase the average lifetime of high-energy electrons, while the Pt SA sites on the S-rich (200) facet served as electron wells on photoexcitation.

## 4. Conclusions

The limited photocatalytic activity of wide bandgap ZnS could be enhanced by controlled Al SA doping for regulating the trap states in the band structure and modulating the electron transport. Owing to the asymmetric single crystalline growth exposing the (200) facet and the change in electron density by lattice expansion, the favorable migration of photoexcited electrons to the S-rich (200) plane provides an additional driving force for immobilization of Pt SA sites onto the basal plane of AZS. Moreover, Al-induced donor levels (shallow defects) can increase the lifetime of photogenerated electrons and improve charge transport. With enhanced photon absorption by the single crystalline AZS planar surface, bulk excitation and transport of electrons to Pt lead to an improved $H_2$ evolution rate of 17.1 mmol $g^{-1}$ $h^{-1}$ under AM1.5G irradiation, which is 33% higher than that of pristine ZS. Pt-AZS achieved an AQY of 34% upon exposure to monochromatic light at 345 nm by using a WB40 UV filter. Further improvement in $H_2$ yield was achieved by irradiating the system in a two-channel photochemical chamber (under UV-A and UV-B exposure), showing a maximum HER rate of 38 mmol $g^{-1}$ $h^{-1}$ for Pt-AZS, which is two times more than that of Pt-ZS. The incorporation of donor levels by Al-doping is achieved without sacrificing the single crystal structure and anisotropy of ZnS. The lack of grain boundaries in single-crystalline AZS with a favorable S-rich surface facilitates the rapid photoexcitation of electrons on the (200) facet from the bulk. This work provides insights into improved photocatalytic $H_2$ evolution by Al-doping in single crystalline photocatalysts, which may modulate the electronic band structure and defect states to achieve a remarkable solar-to-hydrogen production efficiency, surpassing previously reported values.

## Author contributions

The manuscript was written through contributions of all authors. All authors have given approval to the final version of the manuscript.

## Conflicts of interest

The authors declare no conflict of interest.

## Data availability

The data that support the findings of this study are available from the corresponding author upon reasonable request.

The data supporting this article have been included as part of the SI. See DOI: **https://doi.org/10.1039/d5ta03793j**.

## Acknowledgements

The authors are grateful to Dr Y.-C. Lee and Ms. P.-Y. Huang (TLS 14A1, NSRRC) for their valuable assistance with IR data analysis. We gratefully acknowledge the support from the National Science and Technology Council (NSTC), Taiwan (grant no. NSTC 113-2639-M-A49-001-ASP and NSTC 114-2639-M-A49-001-ASP) and the Center for Emergent Functional Matter Science of National Yang-Ming Chiao-Tung University (NYCU) through the Featured Areas Research Center Program within the framework of the Higher Education Sprout Project by the Ministry of Education (MOE) in Taiwan.

## References

1 W. H. Lee, C. W. Lee, G. D. Cha, B.-H. Lee, J. H. Jeong, H. Park, J. Heo, M. S. Bootharaju, S.-H. Sunwoo, J. H. Kim, K. H. Ahn, D.-H. Kim and T. Hyeon, *Nat. Nanotechnol.*, 2023, **18**, 754–762.
2 Y. Chen, L. Soler, C. Cazorla, J. Oliveras, N. G. Bastús, V. F. Puntes and J. Llorca, *Nat. Commun.*, 2023, **14**, 6165.
3 J. Ding, W. Yan, S. Sun, J. Bao and C. Gao, *ACS Appl. Mater. Interfaces*, 2014, **6**, 12877–12884.
4 B. Dai, J. Fang, Y. Yu, M. Sun, H. Huang, C. Lu, J. Kou, Y. Zhao and Z. Xu, *Adv. Mater.*, 2020, **32**, 1906361.
5 T. Hisatomi and K. Domen, *Nat. Catal.*, 2019, **2**, 387–399.
6 Z. Lian, Z. Li, F. Wu, Y. Zhong, Y. Liu, W. Wang, J. Zi and W. Yang, *Commun. Chem.*, 2022, **5**, 93.
7 Z. Wang, Y. Luo, T. Hisatomi, J. J. M. Vequizo, S. Suzuki, S. Chen, M. Nakabayashi, L. Lin, Z. Pan, N. Kariya, A. Yamakata, N. Shibata, T. Takata, K. Teshima and K. Domen, *Nat. Commun.*, 2021, **12**, 1005.
8 Z. Fang, S. Weng, X. Ye, W. Feng, Z. Zheng, M. Lu, S. Lin, X. Fu and P. Liu, *ACS Appl. Mater. Interfaces*, 2015, **7**, 13915–13924.
9 C.-W. Tsao, S. Narra, J.-C. Kao, Y.-C. Lin, C.-Y. Chen, Y.-C. Chin, Z.-J. Huang, W.-H. Huang, C.-C. Huang, C.-W. Luo, J.-P. Chou, S. Ogata, M. Sone, M. H. Huang, T.-F. M. Chang, Y.-C. Lo, Y.-G. Lin, E. W.-G. Diau and Y.-J. Hsu, *Nat. Commun.*, 2024, **15**, 413.
10 J. He, B. Li, J. Yu, L. Qiao, S. Li, X. Zu and X. Xiang, *Opt. Mater.*, 2020, **108**, 110231.
11 S. Wang, Y. Wang, S. L. Zhang, S.-Q. Zang and X. W. (David) Lou, *Adv. Mater.*, 2019, **31**, 1903404.
12 Y. Sun, F. Wang, Y. Fu, C. Chen, X. Wang, Z. Xiao, Y. Liu, J. Xu, B. Li and L. Wang, *RSC Adv.*, 2020, **10**, 812–817.
13 B. Poornaprakash, P. Puneetha, M. S. P. Reddy, S. Sangaraju, P. Rosaiah, B. A. Al-Asbahi, D.-Y. Lee and Y. L. Kim, *J. Mater. Sci.: Mater. Electron.*, 2023, **34**, 1614.
14 A. Wu, L. Jing, J. Wang, Y. Qu, Y. Xie, B. Jiang, C. Tian and H. Fu, *Sci. Rep.*, 2015, **5**, 8858.
15 R. J. Vimal Michael, J. Theerthagiri, J. Madhavan, M. J. Umapathy and P. T. Manoharan, *RSC Adv.*, 2015, **5**, 30175–30186.
16 H. Moon, M. S. Goh, M. Cha, U.-S. Kim, H. S. Whang, N. Son and M. Kang, *Appl. Surf. Sci.*, 2022, **606**, 154787.
17 L. Tie, S. Yang, C. Yu, H. Chen, Y. Liu, S. Dong, J. Sun and J. Sun, *J. Colloid Interface Sci.*, 2019, **545**, 63–70.
18 J. Dong, W. Fang, W. Xia, Q. Lu and X. Zeng, *RSC Adv.*, 2021, **11**, 21642–21650.
19 S. A. Thomas, N. Roy, W. Sharaf Saeed, A. Sreedhar and J. Cherusseri, *Int. J. Hydrogen Energy*, DOI: **10.1016/j.ijhydene.2023.06.302**.

 

20 B. Poornaprakash, U. Chalapathi, P. T. Poojitha, S. V. P. Vattikuti and M. S. P. Reddy, *J. Mater. Sci.: Mater. Electron.*, 2019, **30**, 9897–9902.
21 A. Es-Smairi, N. Fazouan, E. H. Atmani, M. Khuili and E. Maskar, *Appl. Phys. A*, 2021, **127**, 698.
22 V. Selvaraj, H. H. Mahboub, U. Ganapathi, S. K. Chandran, W. Al-Onazi, A. M. Al-Mohaimeed, T.-W. Chen, C. Faggio and B. Paulraj, *Environ. Sci. Pollut. Res.*, 2022, **29**, 73528–73541.
23 N. Bansal, G. C. Mohanta and K. Singh, *Ceram. Int.*, 2017, **43**, 7193–7201.
24 X. Wang, X. Wang, J. Huang, S. Li, A. Meng and Z. Li, *Nat. Commun.*, 2021, **12**, 4112.
25 L. Bao, Y. Jia, X. Ren, X. Liu, C. Dai, S. Ali, M. Bououdina, Z. Lu and C. Zeng, *J. Mater. Sci. Technol.*, 2024, **199**, 75–85.
26 B. Xiao, T. Lv, T. Zhou, J. Zhao, X. Kuang, Y. Zhang, D. Wang, J. Zhang, Z. Zhu and Q. Liu, *ACS Catal.*, 2023, **13**, 12904–12916.
27 M. Hafeez, B. A. Al-Asbahi, M. H. Hj Jumali, M. Yahaya, F. Inam, M. F. Bhopal and A. S. Bhatti, *Mater. Sci. Semicond. Process.*, 2020, **117**, 105193.
28 A. Kudo and M. Sekizawa, *Chem. Commun.*, 2000, 1371–1372.
29 M. Kimi, L. Yuliati and M. Shamsuddin, *J. Nanomater.*, 2015, **2015**, 195024.
30 X. Shi, C. Dai, X. Wang, J. Hu, J. Zhang, L. Zheng, L. Mao, H. Zheng and M. Zhu, *Nat. Commun.*, 2022, **13**, 1287.
31 J. Zhang, Y. Wang, J. Zhang, Z. Lin, F. Huang and J. Yu, *ACS Appl. Mater. Interfaces*, 2013, **5**, 1031–1037.
32 M. M. Khan and K. O. Abdulwahab, *Mater. Sci. Semicond. Process.*, 2024, **181**, 108634.
33 V. S. Bhat, T. S. Tilakraj, M. K. Patil, V. Pujari, B. G. Mulimani and S. R. Inamdar, *J. Mol. Liq.*, 2024, **396**, 123937.
34 I. Daskalakis, I. Vamvasakis, I. T. Papadas, S. Tsatsos, S. A. Choulis, S. Kennou and G. S. Armatas, *Inorg. Chem. Front.*, 2020, **7**, 4687–4700.
35 L. Bao, Y. Dong, C. Dai, G. Xu, Y. Yang, X. liu, D. Ma, Y. Jia and C. Zeng, *Inorg. Chem.*, 2021, **60**, 15712–15723.
36 A. Azmand and H. Kafashan, *J. Alloys Compd.*, 2019, **779**, 301–313.
37 A. Azmand and H. Kafashan, *J. Alloys Compd.*, 2019, **779**, 301–313.
38 T. Takata, J. Jiang, Y. Sakata, M. Nakabayashi, N. Shibata, V. Nandal, K. Seki, T. Hisatomi and K. Domen, *Nature*, 2020, **581**, 411–414.
39 G. Jia, F. Sun, T. Zhou, Y. Wang, X. Cui, Z. Guo, F. Fan and J. C. Yu, *Nat. Commun.*, 2024, **15**, 4746.
40 A. Es-Smairi, N. Fazouan, E. H. Atmani, M. Khuili and E. Maskar, *Appl. Phys. A*, 2021, **127**, 698.
41 G. Kresse and J. Furthmüller, *Phys. Rev. B*, 1996, **54**, 11169–11186.
42 C. S. Pathak, D. D. Mishra, V. Agarwala and M. K. Mandal, *Ceram. Int.*, 2012, **38**, 5497–5500.
43 G. Zhu, S. Zhang, Z. Xu, J. Ma and X. Shen, *J. Am. Chem. Soc.*, 2011, **133**, 15605–15612.
44 X. Zhu, B. Cheng, J. Yu and W. Ho, *Appl. Surf. Sci.*, 2016, **364**, 808–814.
45 J. N. Tiwari, S. Sultan, C. W. Myung, T. Yoon, N. Li, M. Ha, A. M. Harzandi, H. J. Park, D. Y. Kim, S. S. Chandrasekaran, W. G. Lee, V. Vij, H. Kang, T. J. Shin, H. S. Shin, G. Lee, Z. Lee and K. S. Kim, *Nat. Energy*, 2018, **3**, 773–782.
46 C. Lee, W. Yang and R. G. Parr, *Phys. Rev. B*, 1988, **37**, 785–789.
47 J. P. Perdew, K. Burke and M. Ernzerhof, *Phys. Rev. Lett.*, 1996, **77**, 3865–3868.
48 A. Tkatchenko, R. A. DiStasio, R. Car and M. Scheffler, *Phys. Rev. Lett.*, 2012, **108**, 236402.
49 A. Kuzmin, M. Dile, K. Laganovska and A. Zolotarjovs, *Mater. Chem. Phys.*, 2022, **290**, 126583.
50 Y. Chen and J. Chen, *Miner. Eng.*, 2010, **23**, 676–684.
51 X. Liu, Y. Zhang, S. Matsushima, T. Sugiyama, H. Hojo and H. Einaga, *ACS Appl. Energy Mater.*, 2022, **5**, 1849–1857.
52 Y. Zhang, J. Zhao, H. Wang, B. Xiao, W. Zhang, X. Zhao, T. Lv, M. Thangamuthu, J. Zhang, Y. Guo, J. Ma, L. Lin, J. Tang, R. Huang and Q. Liu, *Nat. Commun.*, 2022, **13**, 58.
53 X. Wu, H. Zhang, J. Dong, M. Qiu, J. Kong, Y. Zhang, Y. Li, G. Xu, J. Zhang and J. Ye, *Nano Energy*, 2018, **45**, 109–117.
54 Z.-H. Xue, D. Luan, H. Zhang and X. W. (David) Lou, *Joule*, 2022, **6**, 92–133.
55 Y. Fan, X. Hao, Y. Shao and Z. Jin, *Adv. Sustainable Syst.*, 2024, **8**, 2300300.
56 H. Krishna Sadhanala, A. Maddegalla and K. K. Nanda, *New J. Chem.*, 2017, **41**, 13742–13746.
57 A. Sanchez-Martinez, J. J. Marin-Perez, O. Ceballos-Sanchez, R. Ruelas, R. Ramírez-Bon, E. R. López-Mena and C. E. Pérez-García, *J. Mater. Sci.: Mater. Electron.*, 2024, **35**, 993.
58 S. Benkoula, O. Sublemontier, M. Patanen, C. Nicolas, F. Sirotti, A. Naitabdi, F. Gaie-Levrel, E. Antonsson, D. Aureau, F.-X. Ouf, S.-I. Wada, A. Etcheberry, K. Ueda and C. Miron, *Sci. Rep.*, 2015, **5**, 15088.
59 G. Simões dos Reis, C. Mayandi Subramaniyam, A. D. Cárdenas, S. H. Larsson, M. Thyrel, U. Lassi and F. García-Alvarado, *ACS Omega*, 2022, **7**, 42570–42581.
60 C.-H. Kuan, Y.-C. Chen, S. Narra, C.-F. Chang, Y.-W. Tsai, J.-M. Lin, G.-R. Chen and E. W.-G. Diau, *ACS Energy Lett.*, 2024, **9**, 2351–2357.
61 A. Abid, P. Rajamanickam and E. Wei-Guang Diau, *Chem. Eng. J.*, 2023, **477**, 146755.
62 X. Wang, B. Liu, S. Ma, Y. Zhang, L. Wang, G. Zhu, W. Huang and S. Wang, *Nat. Commun.*, 2024, **15**, 2600.
63 M. Öztaş, M. Bedir, A. Necmeddin Yazici, E. Vural Kafadar and H. Toktamış, *Phys. Rev. B:Condens. Matter Mater. Phys*, 2006, **381**, 40–46.